CrossMark

J. Fluid Mech. (2018), *vol.* 839, *pp.* 387–407. © Cambridge University Press 2018
doi:10.1017/jfm.2018.21

Internal solitary wave generation by tidal flow over topography

R. Grimshaw[1,†] **and K. R. Helfrich**[2]

[1]Department of Mathematics, University College London, WC1E 6BT, UK

[2]Department of Physical Oceanography, Woods Hole Oceanographic Institution, Woods Hole, MA 02543, USA

(Received 14 August 2017; revised 20 December 2017; accepted 21 December 2017; first published online 29 January 2018)

Oceanic internal solitary waves are typically generated by barotropic tidal flow over localised topography. Wave generation can be characterised by the Froude number $F = U/c_0$, where U is the tidal flow amplitude and c_0 is the intrinsic linear long wave phase speed, that is the speed in the absence of the tidal current. For steady tidal flow in the resonant regime, $\Delta_m < F - 1 < \Delta_M$, a theory based on the forced Korteweg–de Vries equation shows that upstream and downstream propagating undular bores are produced. The bandwidth limits $\Delta_{m,M}$ depend on the height (or depth) of the topographic forcing term, which can be either positive or negative depending on whether the topography is equivalent to a hole or a sill. Here the wave generation process is studied numerically using a forced Korteweg–de Vries equation model with time-dependent Froude number, $F(t)$, representative of realistic tidal flow. The response depends on $\Delta_{max} = F_{max} - 1$, where F_{max} is the maximum of $F(t)$ over half of a tidal cycle. When $\Delta_{max} < \Delta_m$ the flow is always subcritical and internal solitary waves appear after release of the downstream disturbance. When $\Delta_m < \Delta_{max} < \Delta_M$ the flow reaches criticality at its peak, producing upstream and downstream undular bores that are released as the tide slackens. When $\Delta_{max} > \Delta_M$ the tidal flow goes through the resonant regime twice, producing undular bores with each passage. The numerical simulations are for both symmetrical topography, and for asymmetric topography representative of Stellwagen Bank and Knight Inlet.

Key words: internal waves, solitary waves, topographic effects

1. Introduction

Although there have been many studies of the propagation of oceanic internal solitary waves (ISW) (see for instance the recent reviews by Holloway, Pelinovsky & Talipova (2001), Helfrich & Melville (2006), Grimshaw, Pelinovsky & Talipova (2007) and Grimshaw *et al.* (2010)), the generation process has been relatively less well studied. Nevertheless the essential characteristics are known, from theory, observations and numerical simulations. In the context of this work, we note especially the many studies in Knight Inlet and other fjords (Farmer & Smith 1980; Farmer

† Email address for correspondence: rgrimshaw@ucl.ac.uk

https://doi.org/10.1017/jfm.2018.21 Published online by Cambridge University Press

& Armi 1999*a*,*b*, 2001; Cummins, Armi & Vagle 2006; Stashchuk & Vlasenko 2007; Cummins & Armi 2010), over Stellwagen Bank in Massachusetts Bay (Lee & Beardsley 1974; Hibiya 1988; Scotti, Beardsley & Butman 2007; Scotti *et al.* 2008; Lai *et al.* 2010) and in the South China Sea (Liu *et al.* 1998, 2004, 2006; Cai, Long & Gan 2002; Orr & Mignerey 2003; Duda *et al.* 2004; Ramp *et al.* 2004; Zhao & Alford 2006; Buijsman, Kanarska & McWilliams 2010; Vlasenko *et al.* 2010; Warn-Varnas *et al.* 2010; Chen *et al.* 2011; Guo *et al.* 2011; Li & Farmer 2011; Vlasenko, Guo & Stashchuk 2012). From these and many other studies we infer that in shallow water, there are essentially just two mechanisms, each involving the interaction of the barotropic tide with a localised topographic feature. One is the generation of an internal tide which steepens as it propagates away from the forcing site, and then generates ISW; this is usually associated with low subcritical Froude numbers, $F = U/c_0 < 1$ where U is the tidal velocity and c_0 is the relevant intrinsic linear long wave speed. This scenario can be modelled with the Korteweg–de Vries (KdV) equation, in which the initial condition are the essentially linear waves formed by the interaction of the tide with the topography. The other is the generation of an upstream propagating undular bore composed of ISW, often developing from an upstream hydraulic jump; this is usually associated with transcritical (or resonant) flow, $F \sim 1$. This scenario can be modelled with the forced Korteweg–de Vries (fKdV) equation, in which the forcing term is provided by the interaction of the tide with a localised topographic feature. There are of course many features specific to each particular location, but these two scenarios would seem to cover most observations when a barotropic tide interacts with a localised topographic feature. There is a third mechanism which operates when a barotropic tide interacts with the topography, generating strong internal tidal beams from a critical point in the slope, which in turn interact with the pycnocline to form ISW (Gerkema 2001; Akylas *et al.* 2007). This case being more associated with deep water scenarios is not our concern here.

However, these fKdV scenarios are usually based on a constant fixed Froude number F whereas in practice this varies, albeit slowly, as the tide varies over a tidal period. Although one might nevertheless expect that each of these scenarios will hold locally in time, as the generation time scale can be expected to be significantly shorter than the tidal period, it is useful to examine how these models behave when the tide, and hence the Froude number F, is allowed to vary slowly in time. This is the purpose of the present paper, where we examine the fKdV model with a time-dependent Froude number, and so with time-dependent forcing. Our aim is to demonstrate within the framework of this model that the generation of large-amplitude ISW occurs near the localised topography when the tide enters the transcritical regime, and that these waves are released upstream as the tide slackens. Surprisingly, there seem to have been relatively few such studies of a time-dependent fKdV equation, although we note the work of Redekopp & You (1995) who reported some numerical simulations in which the F was varied in the transcritical range, but the topographic forcing was kept constant. Pertinently Stastna & Peltier (2004, 2005) made comparisons between the fKdV model and numerical simulations of the full nonlinear equation for time-dependent flow over localised topography resembling Knight Inlet. Although they found that internal wave breaking near the topographic forcing region prevented direct quantitative comparisons with the fKdV model, they did conclude that the upstream propagating ISW were generated when the tidal flow is in the transcritical regime.

In § 2 we present a summary of the fKdV equation and the relevant solution scenarios when F is a constant, and speculate how these scenarios can be used to

https://doi.org/10.1017/jfm.2018.21 Published online by Cambridge University Press

describe the case when F varies. Then in § 3 we present some numerical simulations when F is allowed to vary slowly in time using parameters derived from a two-layer fluid model and a localised symmetric topographic forcing. In § 4 we extend these simulations to representations of some well-known actual observed cases of ISW generation characterised by asymmetric topography. We conclude in § 5.

2. Forced Korteweg–de Vries equation

The asymptotic derivation of the fKdV equation for internal waves was first given by Grimshaw & Smyth (1986) and Melville & Helfrich (1987), and its relevant solutions can be found there, and in many other works. For a recent review see Grimshaw (2010). The outcome is briefly summarised here. At the leading order we get linear long wave theory,

$$\zeta \sim A(x,t)\phi(z) + \cdots, \tag{2.1}$$

where ζ is the vertical particle displacement relative to the basic state, defined by the background density field $\rho_0(z)$ and background current $u_0(z)$. The modal function $\phi(z)$ satisfies the system

$$\{\rho_0(c-u_0)^2\phi_z\}_z + \rho_0 N^2\phi = 0, \quad \rho_0 N^2 = -g\rho_{0z}, \quad \text{for} \quad -h < z < 0, \tag{2.2}$$

$$\phi = 0 \quad \text{at } z = -h, \quad (c-u_0)^2\phi_z = g\phi \quad \text{at } z = 0. \tag{2.3a,b}$$

In general this has an infinite set of solutions for $\phi(z)$ and the linear long wave speed c, but for oceanic internal waves it is customary to examine only mode one which has the fastest internal wave speed (formally the lowest mode zero is the surface wave mode with speed $c \approx (gh)^{1/2}$ in the absence of background current). As usual we normalise ϕ so that $\phi(z_m) = 1$ where $z = z_m$ is the location of the extremum of ϕ. Then the fKdV equation, written in the reference frame of the topography, given by $z = -h + b(x)$, is

$$-A_t - cA_x + \mu AA_x + \delta A_{xxx} + \gamma b_x(x) = 0. \tag{2.4}$$

$$\left.\begin{aligned} I\mu &= 3\int_{-h}^{0} \rho_0(c-u_0)^2\phi_z^3 \,\mathrm{d}z, \\ I\delta &= \int_{-h}^{0} \rho_0(c-u_0)^2\phi^2 \,\mathrm{d}z, \\ I\gamma &= \rho_0 u_0(u_0-c)\phi_z, \quad \text{at } z = -h, \\ I &= 2\int_{-h}^{0} \rho_0(u_0-c)\phi_z^2 \,\mathrm{d}z. \end{aligned}\right\} \tag{2.5}$$

At resonance (that is, at criticality, see below in the next paragraph), $c = \Delta \approx 0$ and this reduces to the more familiar form

$$-A_t - \Delta A_x + \mu_0 AA_x + \delta_0 A_{xxx} + \gamma_0 b_x(x) = 0; \tag{2.6}$$

https://doi.org/10.1017/jfm.2018.21 Published online by Cambridge University Press

$$\left.\begin{aligned} I_0\mu_0 &= 3\int_{-h}^{0}\rho_0 u_0^2\phi_z^3\,\mathrm{d}z,\\ I_0\delta_0 &= \int_{-h}^{0}\rho_0 u_0^2\phi^2\,\mathrm{d}z,\\ I_0\gamma_0 &= \rho_0 u_0^2\phi_z, \quad \text{at } z=-h,\\ I_0 &= 2\int_{-h}^{0}\rho_0 u_0\phi_z^2\,\mathrm{d}z. \end{aligned}\right\} \tag{2.7}$$

Here the modal function ϕ is evaluated at $c=0$, but $c=\Delta$ is retained in the leading-order terms to ensure that all terms remain in balance.

It is now useful to consider the special case when $u_0=U=\text{const}$. Then the speed $c=U-c_0$ where c_0 is the intrinsic linear long wave speed, that is the speed in the absence of a background flow. In that case $c=c_0(F-1)$ where $F=U/c_0$ is the Froude number, and the modal equation becomes

$$c_0^2\{\rho_0\phi_z\}_z+\rho_0 N^2\phi=0, \quad \text{for } -h<z<0, \tag{2.8}$$

$$\phi=0 \quad \text{at } z=-h, \quad c_0^2\phi_z=g\phi \quad \text{at } z=0. \tag{2.9a,b}$$

The coefficients become, to leading order,

$$\left.\begin{aligned} I_0\mu_0 &= 3\int_{-h}^{0}\rho_0 c_0^2\phi_z^3\,\mathrm{d}z,\\ I_0\delta_0 &= \int_{-h}^{0}\rho_0 c_0^2\phi^2\,\mathrm{d}z,\\ I_0\gamma_0 &= \rho_0 c_0 U\phi_z, \quad \text{at } z=-h,\\ I_0 &= 2\int_{-h}^{0}\rho_0 c_0\phi_z^2\,\mathrm{d}z. \end{aligned}\right\} \tag{2.10}$$

When U varies temporally, the coefficients μ_0, δ_0 remain constant, and in the fKdV equation (2.4), only the coefficients $c=U-c_0=c_0(F-1)$ and γ_0 vary, where

$$\gamma_0=F\sigma_0, \quad I_0\sigma_0=\rho_0 c_0^2\phi_z, \quad \text{at } z=-h. \tag{2.11a,b}$$

Next, rescale by

$$\tilde{A}=\frac{\mu_0 A}{6c_0}, \quad \tilde{\Delta}=\frac{c}{c_0}, \quad \tilde{t}=\left\{\frac{c_0^3}{\delta_0}\right\}^{1/2}t, \quad \tilde{x}=\left\{\frac{c_0}{\delta_0}\right\}^{1/2}x, \quad \tilde{b}=\frac{\sigma_0\mu_0 b}{6c_0^2}, \tag{2.12a–e}$$

so that (2.6) adopts the non-dimensional canonical form, after removing the tilde superscript,

$$-A_t-\Delta A_x+6AA_x+A_{xxx}+Fb_x(x)=0, \quad F=1+\Delta. \tag{2.13}$$

For mode one, since ϕ has a positive extremum, $\sigma_0>0$ and so the forcing is positive when $\mu_0 b>0$ but negative when $\mu_0 b<0$. In particular, flow of a two-layer fluid with a near-surface pycnocline over a sill is equivalent to negative forcing.

https://doi.org/10.1017/jfm.2018.21 Published online by Cambridge University Press

The solutions fall into three categories (see Grimshaw & Smyth 1986 and Grimshaw 2010): subcritical $\Delta < \Delta_m < 0$, transcritical $\Delta_m < \Delta < \Delta_M$ and supercritical $\Delta > \Delta_M > 0$. Here the regime boundaries $\Delta_{m,M}$ depend on the forcing. For the asymptotic limit of broad forcing, also known as the hydraulic limit,

$$\Delta_{M,m} = \pm\{12F|b_M|\}^{1/2}, \tag{2.14}$$

where b_M is the maximum obstacle displacement and is positive when $b > 0$, or negative when $b < 0$. In the usual fKdV limit, we can set $F \approx 1$ here, but using the relation $F = 1 + \Delta$ a refinement is

$$\Delta_{M,m} = 6|b_M| \pm \{12|b_M| + 36b_M^2\}^{1/2}. \tag{2.15}$$

Thus the supercritical boundary is increased and the subcritical boundary is decreased.

The subcritical and supercritical regimes are essentially linear and near the obstacle in a steady state. They are given by the approximate expressions valid for large $|\Delta|$ and as $t \to \infty$,

$$A \sim \frac{Fb}{\Delta} + H(x)\frac{Fb_m}{|\Delta|^{1/2}} \sin\left(|\Delta|^{1/2}x\right), \quad \Delta \to -\infty, \quad b_m = \int_{-\infty}^{\infty} b(x)\,\mathrm{d}x, \tag{2.16}$$

$$A \sim \frac{Fb}{\Delta}, \quad \Delta \to \infty. \tag{2.17}$$

Here $H(x)$ is the Heaviside function. The subcritical solution (2.16) is obtained by solving the steady-state linearised form of the fKdV equation (2.13), while for the supercritical solution (2.17) the exponential decay away from the localised forcing is omitted as this occurs on a very short length scale $\Delta^{-1/2}$. Note that in (2.16) $\Delta = F - 1$ is bounded from below by $F = 0$. Close to the regime boundaries, the nonlinear terms provide corrections, and in particular the sinusoidal lee waves in (2.16) are replaced with cnoidal waves. In the transcritical regime, for positive forcing, the solution consists of a steady hydraulic solution over the obstacle, terminating with an upstream elevation resolved by an upstream propagating undular bore, and a downstream depression terminated by a downstream propagating undular bore. Figure 1 shows a numerical solution of (2.13) with $b_M = 0.01$ and $\Delta = 0$. The constant forcing is started impulsively with $A(x, 0) = 0$. Details of the numerical scheme are discussed below. As Δ increases towards Δ_M the upstream undular bore resembles more a sequence of solitary waves, and the downstream undular bore weakens, and as Δ decreases towards Δ_m the upstream undular bore weakens, and the downstream undular bore intensifies. For negative forcing, the same scenario occurs upstream and downstream, but the flow over the obstacle remains unsteady, and there is some modulation of the upstream and downstream undular bores as illustrated in figure 2 for $b_M = -0.01$ and constant $\Delta = 0$.

3. Generation of internal undular bores by tidal interaction with symmetric topography

The generation of internal undular bores by tidal flow can now be modelled by supposing that Δ varies slowly with time. Suppose for instance that Δ increases from a large negative value (formally $\Delta = -1$ where $F = 0$) to a maximum value of Δ_{max} and then decreases back again, modelling the onset of an increasing tidal current followed by a decreasing tidal current, both in the same positive x-direction. Then three scenarios can be identified.

https://doi.org/10.1017/jfm.2018.21 Published online by Cambridge University Press

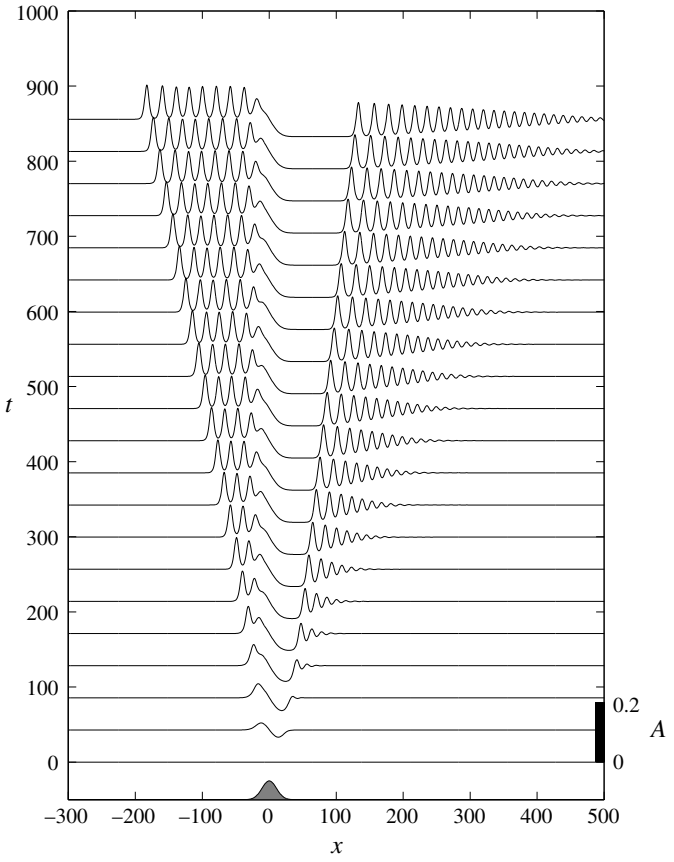


FIGURE 1. Numerical solution of the fKdV equation (2.13) for a localised obstacle, with $b_M = 0.01$ and $\Delta = 0$. The location and shape of the topography (arbitrary amplitude) is shown at the bottom of the plot.

(i) If $\Delta_{max} < \Delta_m$ then the flow is always subcritical. On the increasing tide lee waves are generated, which reach a maximum amplitude at Δ_{max}. These waves cannot be maintained as Δ decreases on the decreasing tide, and so propagate over the obstacle and then upstream.

(ii) If $\Delta_m < \Delta_{max} < \Delta_M$ the flow reaches criticality at its peak. During the peak period, internal undular bores propagate slowly both upstream and downstream. But as the tide recedes, the upstream and downstream undular bores propagate back upstream. This could be identified as the Maxworthy mechanism (Maxworthy 1979). In his laboratory experiment a large depression formed in the lee of the obstacle when the tidal flow reached criticality. As the tidal flow slackened the depression moved back upstream and evolved into several internal solitary waves.

(iii) If $\Delta_{max} > \Delta_M$ the flow passes through the transcritical regime as the tide develops, passes into the supercritical regime at the peak tide, and then again passes through the transcritical regime as it weakens. In this case the strongest internal undular bores are generated in the middle stage as the tide strengthens and then again at the middle stage as the tide weakens. On the growing tide

https://doi.org/10.1017/jfm.2018.21 Published online by Cambridge University Press

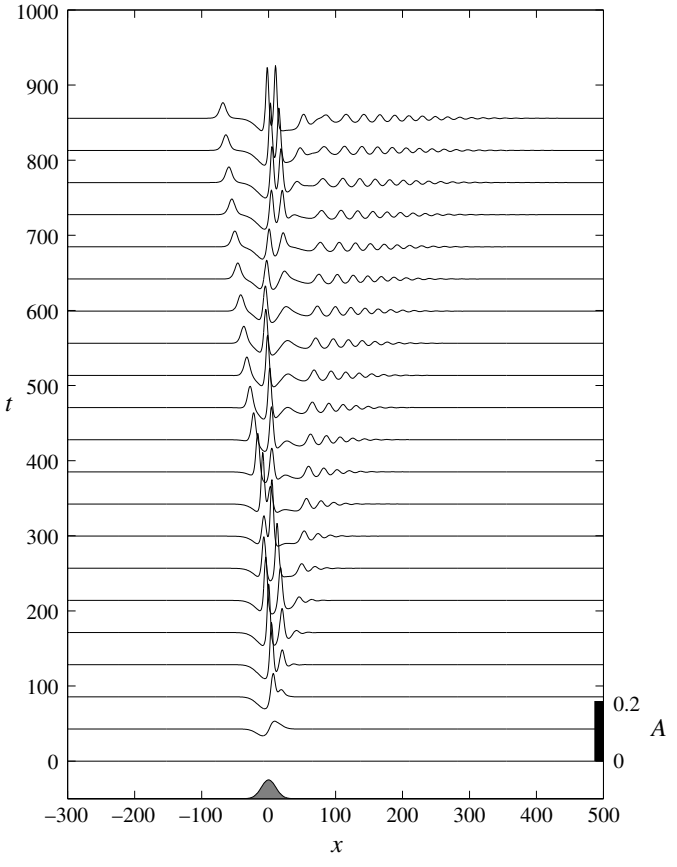


FIGURE 2. The same as figure 1 but now for $b_M = -0.01$.

these undular bores are swept downstream as the peak tide is approached, but propagate back upstream as the tide weakens.

We next present some numerical solutions for time-dependent forcing $F(t)$. We consider the specific case of sinusoidal barotropic tidal flow

$$\Delta = F_{max}\sin(\omega t) - 1, \tag{3.1}$$

over half of a tidal cycle, $0 \leqslant t \leqslant \pi/\omega$, where ω is the tidal frequency. This forcing may pass through the resonant regime on both the acceleration and deceleration phase, may reside in the resonant regime for an extended period, or may not be large enough to enter the resonant regime, depending on $\Delta_{max} = F_{max} - 1$ and $\Delta_{M,m}$ from (2.15) (or (2.14)). Figures 3 and 4 show, respectively, an example of these three possibilities for $b_M = 0.03$ and the resonant band $1 + \Delta_{M,m}$ from (2.15).

Using (2.12) the scaled frequency $\tilde{\omega} = \omega(\delta/c_0^3)^{1/2}$ (re-introducing the tildes). With the (dimensional) topography

$$b(x) = b_M s(x), \tag{3.2}$$

https://doi.org/10.1017/jfm.2018.21 Published online by Cambridge University Press

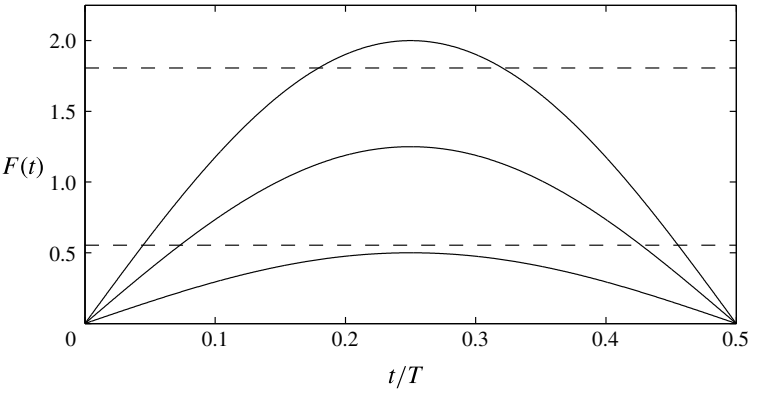


FIGURE 3. $F(t)$ from (3.1) for $F_{max} = 0.5$, 1.25 and 2. Here $T = 2\pi/\omega$. The dashed lines indicate the resonant regime from (2.15) for $|b_M| = 0.03$.

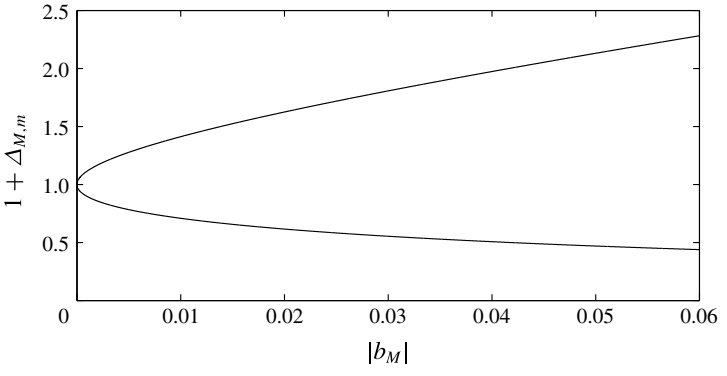


FIGURE 4. The resonant band limits $1 + \Delta_{M,m}$ from (2.15).

where $s(x)$ is a shape function with $\max(s) = 1$ and b_M is the amplitude, the forcing term in (2.13) becomes

$$F(\tilde{t})\tilde{b}_{\tilde{x}} = F(\tilde{t})\tilde{b}_M s_{\tilde{x}}, \quad \text{where } \tilde{b}_M = \frac{\sigma_0 \mu_0 b_M}{6c_0^2}. \tag{3.3}$$

Estimates for the non-dimensional parameters $\tilde{\omega}$ and $\tilde{b}_M$ are found by considering a Boussinesq, two-layered stratification with layer depths h_i and densities ρ_i in each layer. Here $i = 1, 2$ indicates the upper and lower layers, respectively. The coefficients (2.10) and (2.11) become

$$\mu_0 = \frac{3}{2} c_0 \frac{h_1 - h_2}{h_1 h_2}, \quad \delta_0 = \frac{c_0}{6} h_1 h_2, \quad \sigma_0 = \frac{c_0}{2} \frac{h_1}{h_1 + h_2} \quad \text{and} \quad c_0 = \left(g' \frac{h_1 h_2}{h_1 + h_2} \right)^{1/2}, \tag{3.4a–d}$$

with $g' = g(\rho_2 - \rho_1)/\rho_1$. Conditions representative of the coastal ocean are total depth $H = h_1 + h_2 = 100$–300 m, $0.1 < h_1/H < 0.5$, $|b_M|/H \lesssim 0.2$, $g' = 0.01$–0.02 m s^{-2} and semi-diurnal tidal frequency $\omega = 1.41 \times 10^{-4}$ s^{-1}. From (2.12), the normalising

https://doi.org/10.1017/jfm.2018.21 Published online by Cambridge University Press

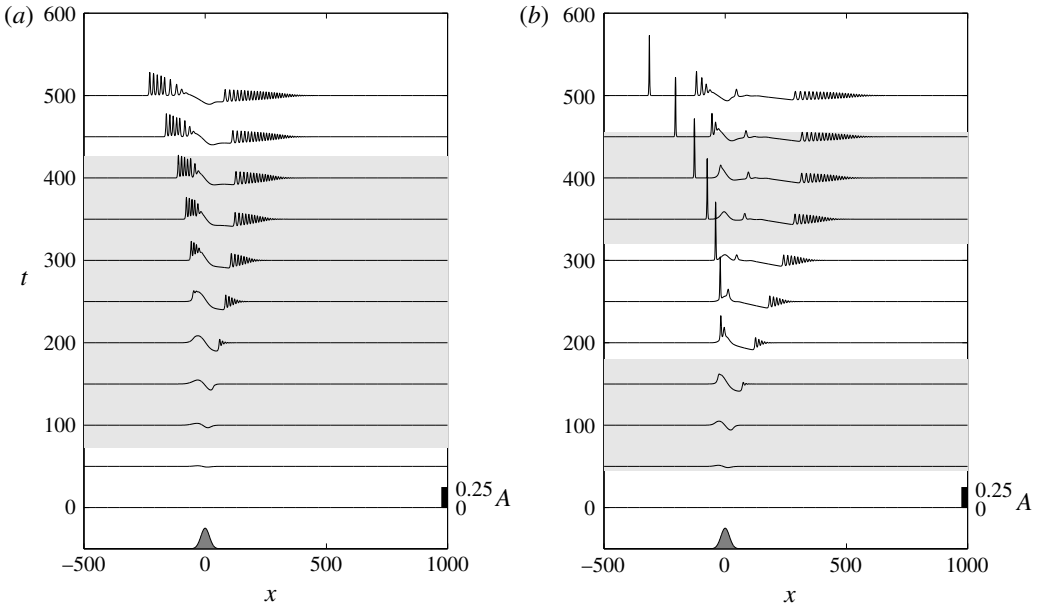


FIGURE 5. (*a*) Solution of (2.13) for $(b_M, T, w_b) = (0.03, 1000, 25)$ with $F_{max} = 1.25$. (*b*) The same but now $F_{max} = 2$. The location and shape of the topography (arbitrary amplitude) is shown at the bottom of the plot. The light grey shading indicates the time when the forcing is in the critical region, $\Delta_m < F(t) - 1 < \Delta_M$, from (2.15) and (3.1).

length scale $(\delta_0/c_0)^{1/2} = 10$–$60$ m and time scale $(\delta_0/c_0^3)^{1/2} = 30$–$70$ s. These parameter ranges give $|\tilde{b}_M| \lesssim 0.05$ and $\tilde{T} = 2\pi/\tilde{\omega} = 700$–$1500$. The topographic shape is taken to be a Gaussian,

$$s(\tilde{x}) = \mathrm{e}^{-(\tilde{x}/\tilde{w}_b)^2}, \tag{3.5}$$

with scaled width $\tilde{w}_b = w_b(c_0/\delta_0)^{1/2} = 25$–$100$ for $w_b/H \approx 5$–10.

Numerical solutions of (2.13) were obtained with a Fourier pseudo-spectral discretisation in x. The nonlinear term was dealiased using the 2/3-rule truncation. Temporal integration employed a third-order, low-storage Runge–Kutta scheme (Williamson 1980). The barotropic forcing was given by (3.1) for $t \leqslant T/2$ and the topographic shape by (3.5). The maximum forcing $F_{max} = 0.5$–2, $T = 600$–1400, $|b_M| \leqslant 0.06$ and $w_b = 25$ and 75 (after again dropping the tildes). The scheme is periodic in x, although the domain size was always taken large enough to avoid end effects. A typical domain had a length of 1500 and used 3072 or 4096 grid cells. A typical time step was 0.001.

Figure 5(*a*) shows the solution $A(x, t)$ for a run with $F_{max} = 1.25$, $T = 1000$, $w_b = 25$ and positive forcing $b_M = 0.03$. Here $\Delta_m < \Delta_{max} < \Delta_M$ from figure 3. The passage of the forcing through the resonance regime excites undular bores upstream and downstream of the topography (centred at $x = 0$) similar to the constant Δ example in figure 1. However the upstream waves are less regularly separated, reflecting the time variation of Δ, and after the forcing peaks (at $t = 250$) the downstream bore begins to move upstream (scenario 2 above). Figure 5(*b*) shows the evolution for $F_{max} = 2$. Here $\Delta_{max} > \Delta_M$ (scenario 3) so the forcing involves distinct acceleration and deceleration passages through the resonant region. This gives rise to a single upstream propagating solitary wave generated on the accelerating phase. A trailing

https://doi.org/10.1017/jfm.2018.21 Published online by Cambridge University Press

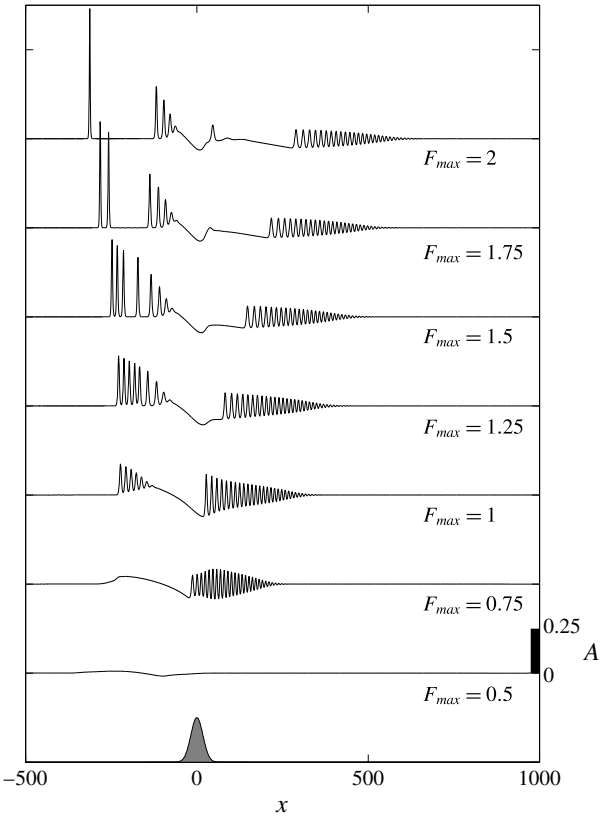


FIGURE 6. $A(x, T/2)$ for $(b_M, T, w_b) = (0.03, 1000, 25)$ and F_{max} as indicated. The location and shape of the topography (arbitrary amplitude) is shown at the bottom of the plot.

packet evolves on the deceleration phase of the forcing from the release of the supercritical-like response over the topography.

The effect of changing F_{max} is summarised in figure 6 where the solutions at the end of the forcing period, $A(x, t = T/2)$, are shown for several $0.5 \leqslant F_{max} \leqslant 2$. The other parameters are unchanged. For $F_{max} = 0.5$ and 0.75, $\Delta_{max} \lesssim \Delta_m$ and the upstream response is weak since the forcing at most just enters the resonant regime for a very brief period (scenario 1). Runs with $F_{max} = 1$, 1.25 and 1.5 ($\Delta_m < \Delta_{max} < \Delta_M$) all produce upstream and downstream bores (scenario 2). When $F_{max} \geqslant 1.75$, $\Delta_{max} \gtrsim \Delta_M$, the upstream response in particular reflects the two passages through resonance (scenario 3).

Solutions for negative forcing $b_M = -0.03$ and $F_{max} = 1.25$ and 2, with $T = 1000$ and $w_b = 25$ unchanged from above, are plotted in figure 7. In both examples the negative forcing results in a downstream undular bore on the increasing phase of the barotropic flow that is released to move upstream as the tidal flow decreases for $t > 250$. Passage of the waves back over the forcing region leads to a more complicated and variable wave field upstream and over the topography than for positive forcing as anticipated from the constant forcing example of figure 2. The effect of further variations in F_{max}, with the other parameters unchanged, on the solutions at $t = T/2$ are shown in figure 8. Again, differences in the response reflect the magnitude of Δ_{max} in comparison to Δ_m and Δ_M.

https://doi.org/10.1017/jfm.2018.21 Published online by Cambridge University Press

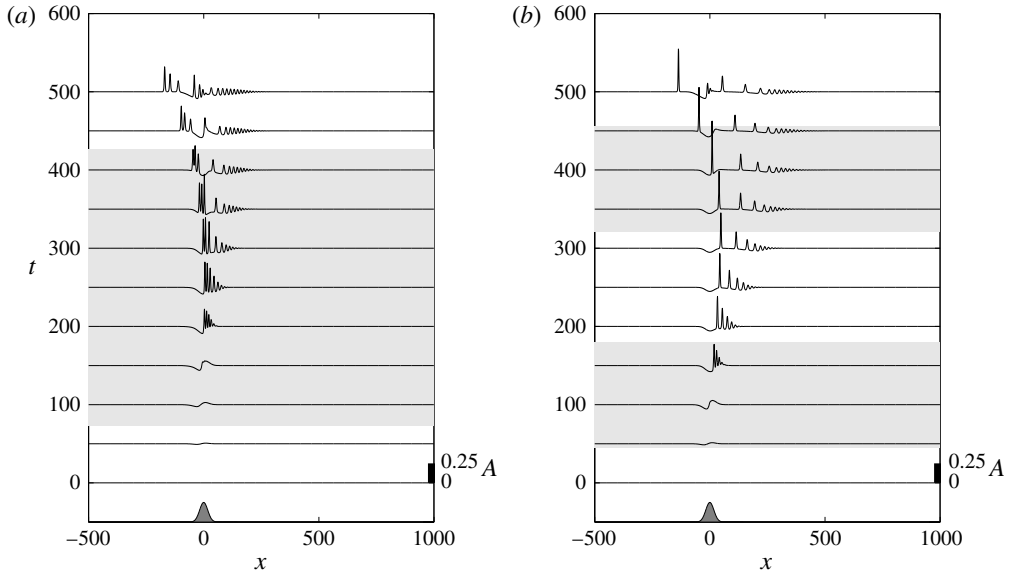


FIGURE 7. The same as figure 5 but now for $b_M = -0.03$. (*a*) $F_{max} = 1.25$. (*b*) $F_{max} = 2$.

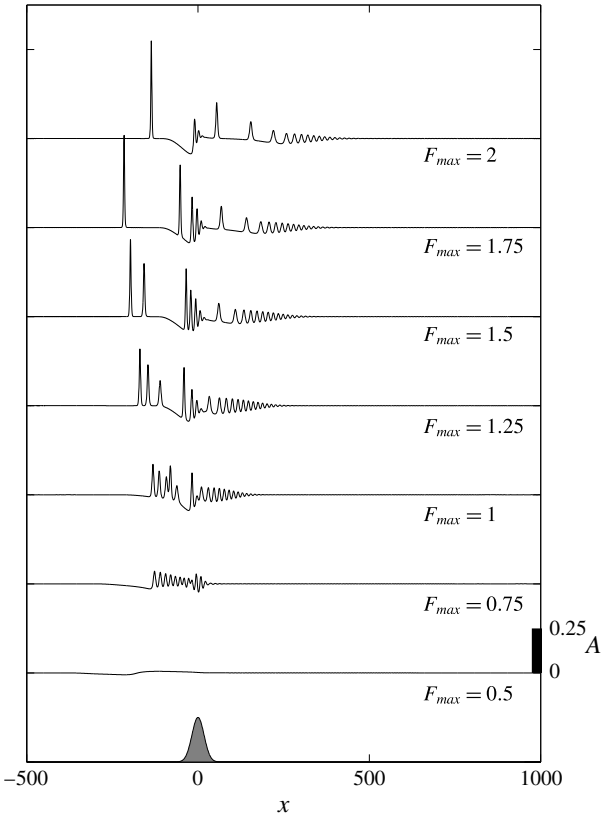


FIGURE 8. $A(x, T/2)$ for $(b_M, T, w_b) = (-0.03, 1000, 25)$ and F_{max} as indicated.

https://doi.org/10.1017/jfm.2018.21 Published online by Cambridge University Press

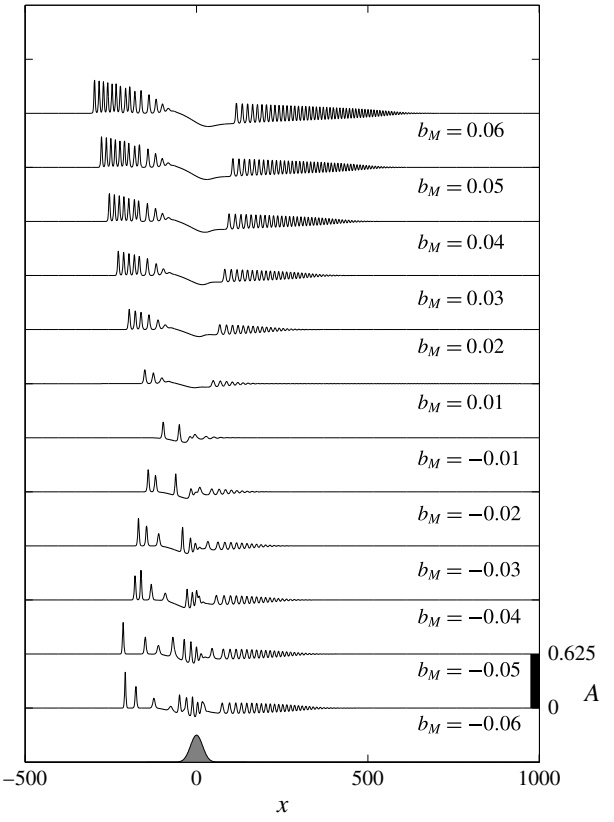


FIGURE 9. $A(x, T/2)$ for $(F_{max}, T, w_b) = (1.25, 1000, 25)$ and b_M as indicated.

The effect of varying the topographic amplitude, b_M, for $F_{max} = 1.25$ ($\Delta_m < \Delta_{max} < \Delta_M$), $T = 1000$ and $w_b = 25$ is shown in figure 9. In addition to the increase of topographic forcing magnitude, increases in $|b_M|$ also lead to increased duration of the barotropic forcing residing within the resonant band, hence larger and more numerous waves are generated.

The effect of forcing duration is further illustrated in figures 10(*a*) and 10(*b*) which show $A(x, T/2)$ for $T = 600$ and 1400, respectively. Here $b_M = 0.03$, $w_b = 25$ and $F_{max} = 0.5$–2. The same results for $b_M = -0.03$ are shown in figure 11.

Figure 12 shows the effect of changing the topographic width scale from $w_b = 25$ to $w_b = 75$ on $A(x, T/2)$ for $b_M = 0.03$. Here $T = 1000$ and $F_{max} = 0.5$–2. This figure should be compared to figure 6 where $w_b = 25$. The broader topography, hence weaker forcing through reduction of s_x, results in a weaker upstream and downstream bores for all F_{max}. However, for negative topographic forcing $b_M = -0.03$ (figure 13), the upstream propagating bore is eliminated, while the downstream response is increased in comparison to the narrower topography, $w_b = 25$, shown in figure 8.

4. Generation of internal undular bores by tidal interaction with asymmetric topography

In order to compare this theory in more detail with the generation at actual sites, we note that in practice the forcing topography is often highly asymmetric. This is

https://doi.org/10.1017/jfm.2018.21 Published online by Cambridge University Press

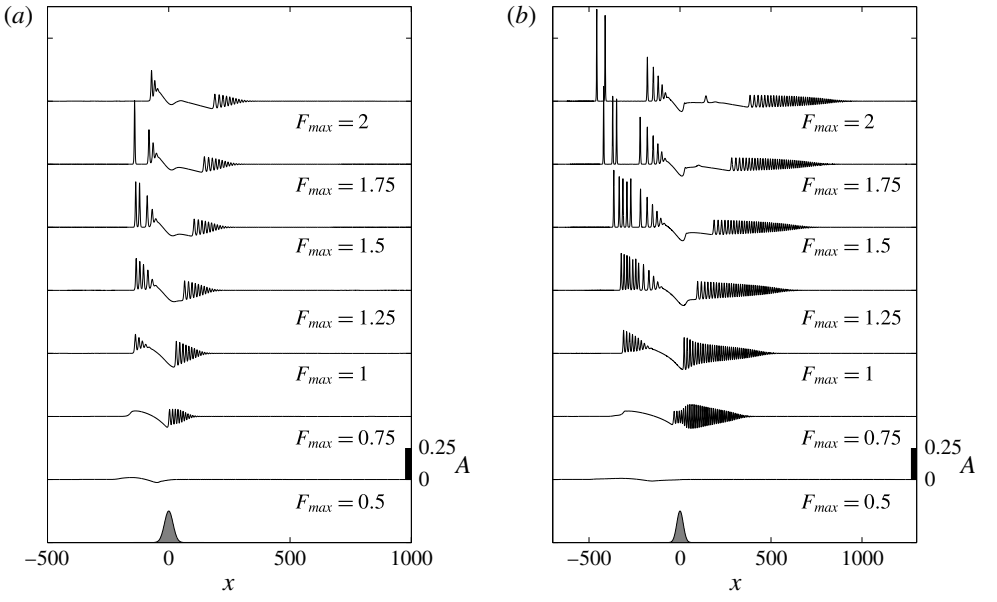


FIGURE 10. (*a*) $A(x, T/2)$ for $(b_M, w_b) = (0.03, 25)$, F_{max} as indicated, and $T = 600$. (*b*) The same but now $T = 1400$.

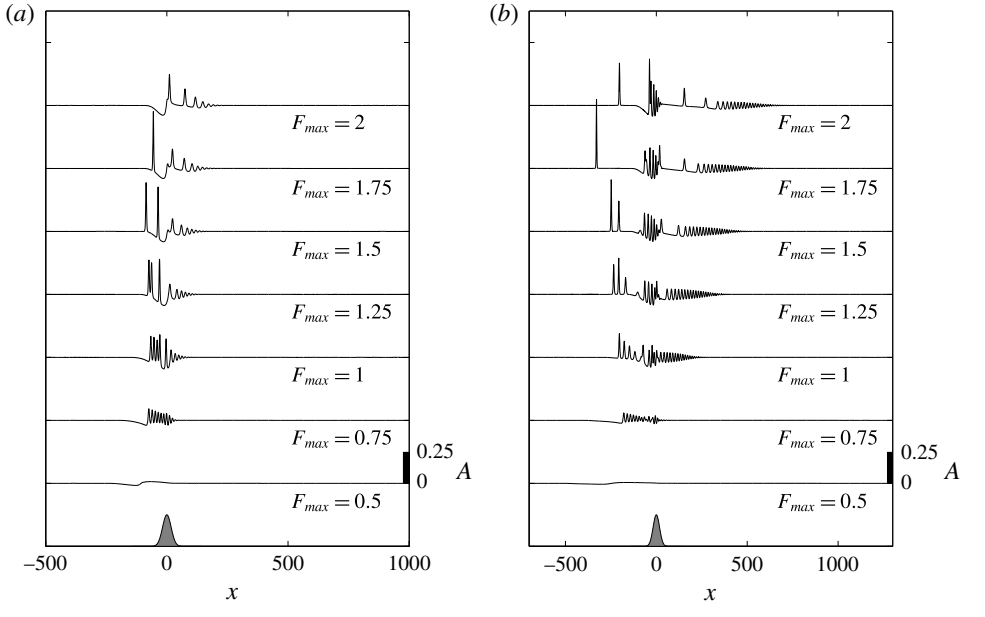


FIGURE 11. (*a*) $A(x, T/2)$ for $(b_M, w_b) = (-0.03, 25)$, F_{max} as indicated, and $T = 600$. (*b*) The same but now $T = 1400$.

the case, for instance, with Stellwagen Bank (Scotti *et al.* 2007, 2008), where the bank is much steeper on the shoreward side than on the ocean side. In figure 14 we show some simulations representing ebb tide for Stellwagen Bank using a model

https://doi.org/10.1017/jfm.2018.21 Published online by Cambridge University Press

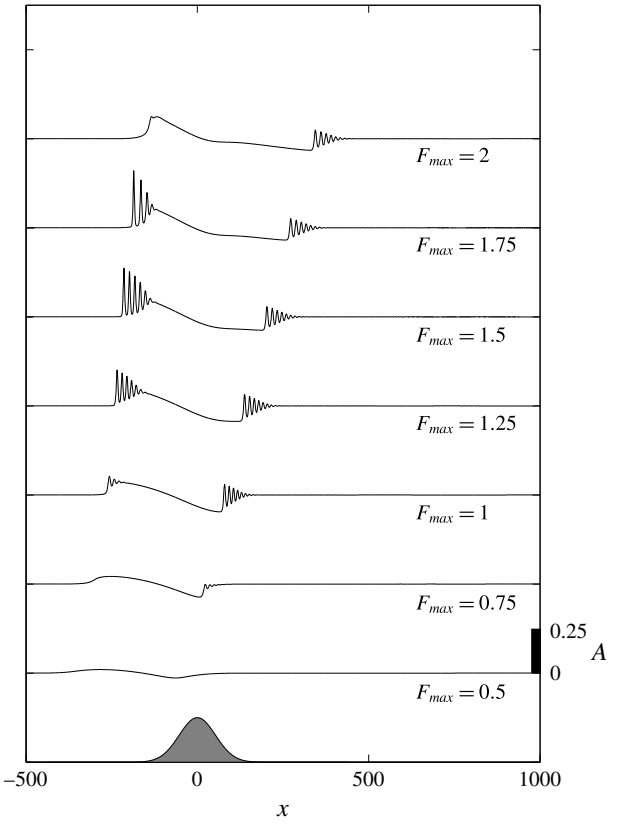


FIGURE 12. $A(x, T/2)$ for $w_b = 75$, $T = 1000$ and $b_M = 0.03$ with F_{max} as indicated.

topography of the same asymmetric shape as the actual topography. The simulations use both the fKdV model (figure 14*a*) with a reduced topographic amplitude and a two-layer shallow water model (figure 14*b*) with the full topography, both shown in the lower panels. The figure shows the interface evolution over the first half-period of tidal forcing, and for an upper layer depth $h_1 = 12.75$ m $= 0.15h$, where the total depth $h = 85$ m and reduced gravity $g' = 0.0196$ ms^{-2}, giving $c_0 = 0.46$ ms^{-1}. The plot is in dimensional units for direct comparison with observations. Because KdV theory is formally limited to small-amplitude topography, the solution in figure 14(*a*) has the topographic amplitude reduced to $b_M = 12.75$ m (15 % of the total depth) from the actual value of $b_M = 55$ m, and $F_{max} = 1.5$. This topography and tidal amplitude place the forcing in scenario 2 since $\Delta_M = 0.54$. For comparison, figure 14(*b*) shows the solution of the two-layer shallow water equations (non-dispersive) for the ebb forcing with the actual topography and a maximum upstream $F = 0.24$. This flow produces a maximum F over the sill of approximately 1.5. The magnitude and direction of the tidal flow is indicated by the heavy lines in each case. Not surprisingly, the two figures show quantitatively different results and note that the shallow water simulations cannot produce the internal waves, but do show the steepening bores that lead to their formation. However, the qualitative features, especially the general shape and timing of the upstream-moving disturbances, are in good agreement, suggesting that the fKdV model is capturing the essential features of the generation process on this ebb phase of the tide.

https://doi.org/10.1017/jfm.2018.21 Published online by Cambridge University Press

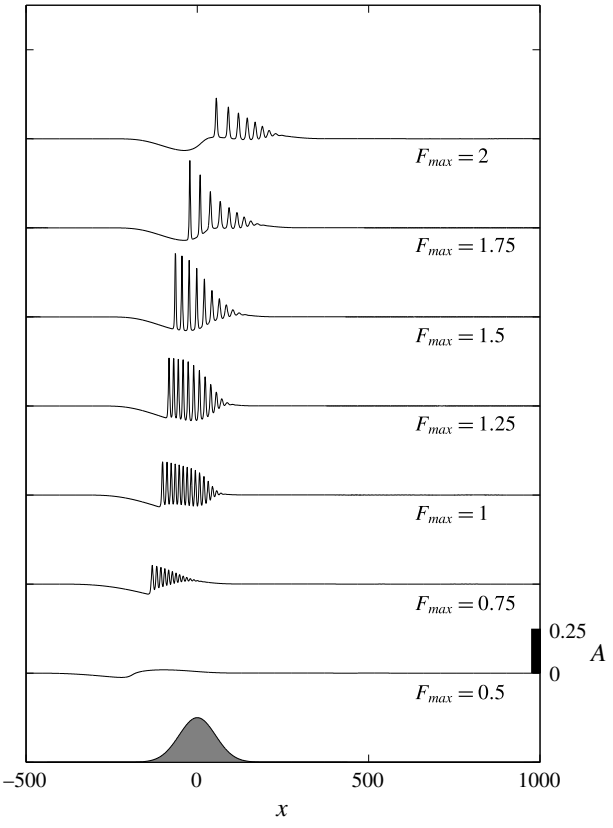


FIGURE 13. $A(x, T/2)$ for $w_b = 75$, $T = 1000$ and $b_M = -0.03$ with F_{max} as indicated.

An equivalent pair of simulations for the Stellwagen Bank flood tide are shown in figure 15. Again, there are quantitative differences between the fKdV and shallow water runs (e.g. the strong downstream jump is absent in the KdV simulation while the upstream waves are not present in the shallow water simulation), but the leading upstream disturbance front, at $x \approx 3$–3.5 km, is captured in both. The effect of the topographic asymmetry leads to substantial changes in the response when compared to the ebb tide examples above.

Knight Inlet is another asymmetrical, tidally forced sill (Farmer & Armi 1999*b*; Armi & Farmer 2002). In figure 16 we show fKdV and shallow water equation simulations for the flood tide. In these calculations the total water depth is taken to be $h = 100$ m. This is less than the actual depth of approximately 350 m, but is about the depth of the downstream flow separation (Armi & Farmer 2002; Cummins *et al.* 2003) on flood tide and is thus a reasonable approximation for the active total depth in a two-layered reduction. Again, the topographic shape replicates the steeper landward side of the sill, over which the water is 60 m deep. For these simulations we use an upper layer depth $h_1 = 12$ m and reduced gravity $g' = 0.076$ ms^{-2}, giving $c_0 = 0.90$ ms^{-1}. Figure 16(*a*) shows the fKdV simulation for $b_M/h = 0.15$ and $F_{max} = 1.5$. The strengthening flood tide generates a wave packet that is trapped just upstream of the sill crest until the tide begins to slacken, after which the waves propagate upstream, in qualitative agreement with observations (Farmer & Armi 1999*a*). In the companion two-layer shallow water simulation in figure 16(*b*)

https://doi.org/10.1017/jfm.2018.21 Published online by Cambridge University Press

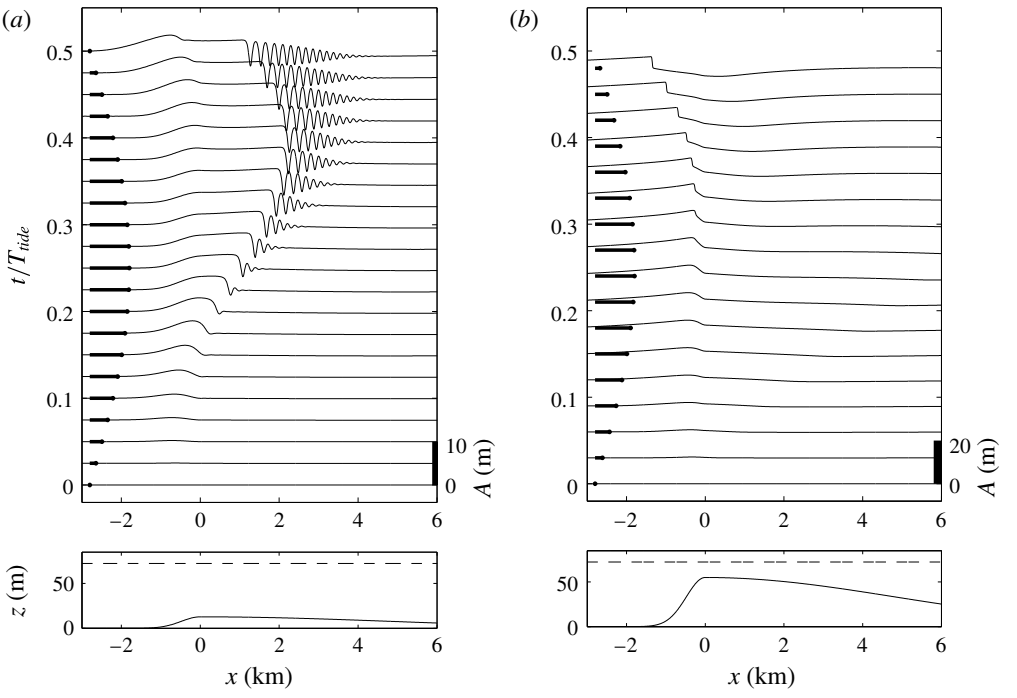


FIGURE 14. (*a*) Numerical solution of the fKdV equation (2.13) for a representation of Stellwagen Bank for an ebb tide with $b_M/h = 0.15$, $h = 85$ m and $F_{max} = 1.5$. (*b*) Numerical solution of the two-layer shallow water equations for a flood tide with the actual topography, $b_M/h = 0.65$, and an maximum upstream $F = 0.24$. The lower panels show the topography and the resting interface position. The upper panels show the interface displacement through the tidal forcing. The magnitude and direction of the barotropic flow are indicated by the heavy lines.

the timing of the upstream disturbance mirrors the waves in the fKdV simulation, although the downstream hydraulic jump is both weaker and shorter lived in the fKdV model. Both simulations highlight the role of a subcritical zone between the upstream jump, or bore, and the hydraulic critical flow at the sill crest, in which the solitary waves develop (Cummins & Armi 2010). The Knight Inlet ebb tide fKdV and shallow water simulations are shown in figure 17. Again the timing of the upstream propagating disturbances are qualitatively similar in both simulations. We note that in the Knight Inlet observations and numerical simulations, the strong flow deformation over the sill crest with local shear instability, mixing and possible formation of a three-layer flow structure (see Farmer & Armi (1999*a*), Cummins *et al.* (2003), Cummins *et al.* (2006) and Cummins & Armi (2010) for instance) is not captured of course, in either the fKdV model or in the two-layer simulations. Nevertheless, the formation of the upstream wave field is at least qualitatively captured, suggesting that this is essentially determined by the passage of the Froude number through criticality as we have described in § 3 and as has been previously suggested by Farmer & Armi (1999*a*) and Stastna & Peltier (2004).

https://doi.org/10.1017/jfm.2018.21 Published online by Cambridge University Press

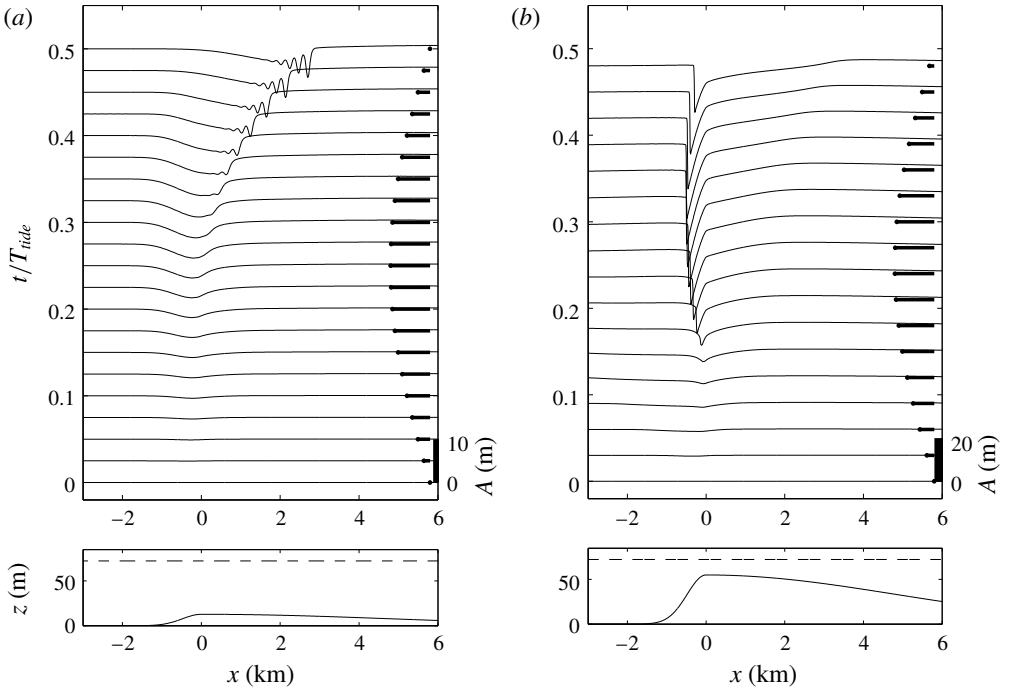


FIGURE 15. The same as figure 14, but now for the flood tide.

5. Discussion

As discussed in the introduction, our focus here is on the generation of ISW by barotropic tidal flow over localised topography for those cases when the tidal flow reaches criticality, or passes through criticality, at the peak stage of the tidal cycle. We are proposing that a suitable model for this scenario is the fKdV equation (2.13), expressed there in scaled canonical form. Unlike most previous studies of the fKdV equation, we allow the Froude number $F = 1 + \Delta$ to vary temporally over half a tidal cycle, from zero to a maximum value F_{max}. Then we have presented in § 3 several simulations for a symmetrical obstacle, where the main parameters varied are F_{max}, b_M (the maximum obstacle height), w_b the obstacle width, and the obstacle polarity. Although there are quantitative differences between these simulations, they all point towards the same conclusion. Nonlinear waves form near the obstacle as the tidal flow passes through criticality, and these are then released upstream in the form of undular bores as the tidal flow weakens towards zero. Because for many actual sites, the topography is not symmetric, in § 4 we presented some simulations for topography representing Stellwagen Bank and the Knight Inlet sill respectively, two heavily observed and modelled sites. Although there are some substantial differences with the results presented in § 3, the same basic conclusion can be reached, that is, large-amplitude waves form near the obstacle at criticality and are released upstream as undular bores as the tidal flow weakens.

We infer that the fKdV model is a very useful resource for modelling and interpreting the formation of internal undular bores generated by tidal flow over localised topography. There are obvious limitations, such as the restriction to weakly nonlinear waves and small-amplitude topography, so that intrinsically this model

https://doi.org/10.1017/jfm.2018.21 Published online by Cambridge University Press

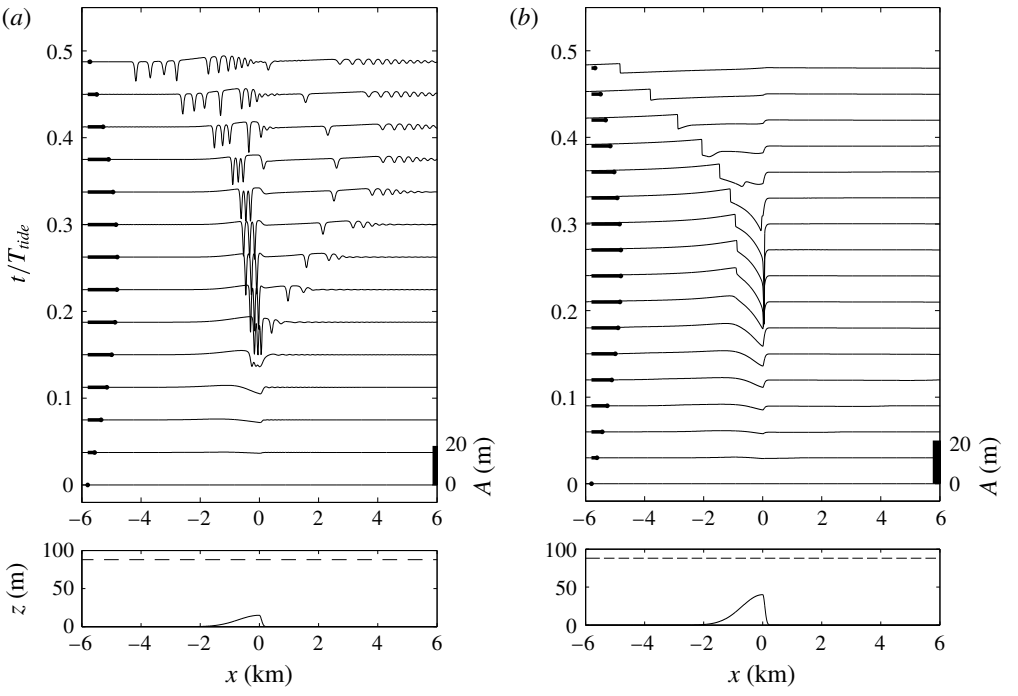


FIGURE 16. (*a*) Numerical solution of the fKdV equation (2.13) for a representation of Knight Inlet sill for a flood tide with $b_M/h = 0.15$, $h = 100$ m and $F_{max} = 1.5$. (*b*) Numerical solution of the two-layer shallow water equations for an ebb tide with the full topography, $b_M/h = 0.4$, and an maximum upstream $F = 0.66$. The lower panels show the topography and the resting interface position. The upper panels show the interface displacement through the tidal forcing. The magnitude and direction of the barotropic flow are indicated by the heavy lines.

cannot describe the turbulence, and mixing produced at the obstacle sometimes seen in observations and in fully nonlinear numerical models. Also the fKdV model is restricted to a single vertical mode (assumed here to be mode one) and so cannot describe the possible generation of higher modes as occasionally observed. Further, like the KdV model, the fKdV model is unidirectional, and captures only the resonant wave. In practice flow interaction with topography will also generate waves propagating rapidly away from the topography, but as they are non-resonant, these can be expected to be usually quite small and have been ignored here. Nonetheless, in spite of these limitations, the fKdV model is able to describe quite well the internal undular bores propagating upstream as the tidal flow slackens. Indeed, the trapping of large internal waves near the topography at criticality, and their release as the tidal flow slackens, would seem to be a very robust process, and essentially independent of the detailed flow structure over the topography itself.

Acknowledgements

R.G. was supported by the Leverhulme Trust through the award of a Leverhulme Emeritus Fellowship. K.R.H. was supported by grant N00014-11-1-0701 from the Office of Naval Research.

https://doi.org/10.1017/jfm.2018.21 Published online by Cambridge University Press

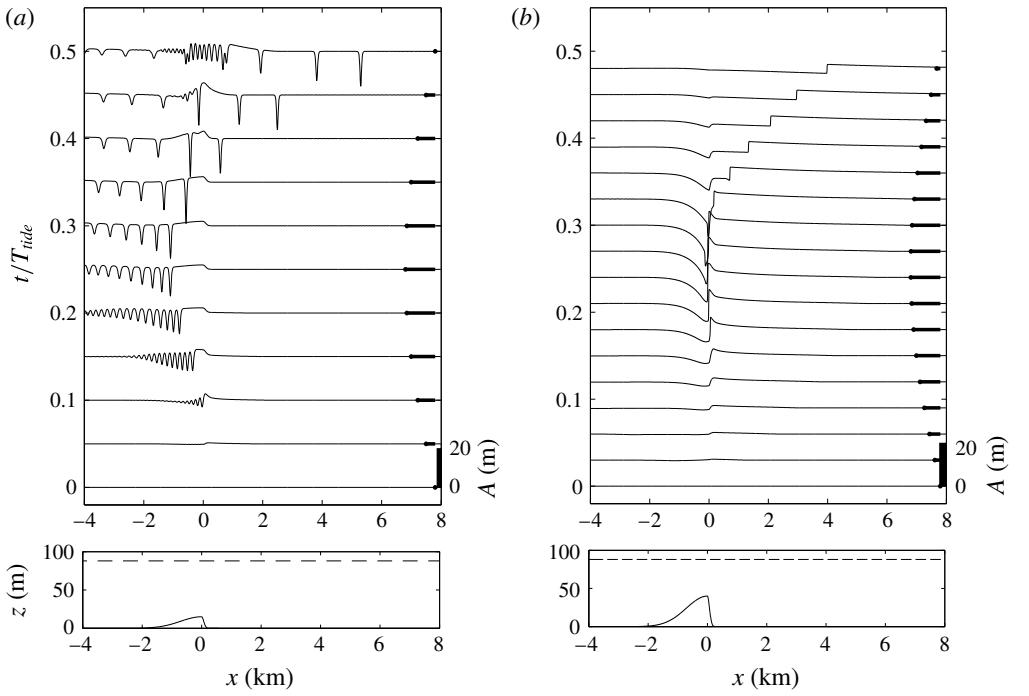


FIGURE 17. The same as figure 16, but now for the ebb tide.

REFERENCES

AKYLAS, T., GRIMSHAW, R., CLARK, S. & TABAEI, A. 2007 Reflecting tidal wave beams and local generation of solitary waves in the ocean thermocline. *J. Fluid Mech.* **593**, 297–313.

ARMI, L. & FARMER, D. 2002 Stratified flow over topography: bifurcation fronts and transition to the uncontrolled state. *Proc. R. Soc. Lond.* A **458**, 513–538.

BUIJSMAN, M. C., KANARSKA, Y. & MCWILLIAMS, J. C. 2010 On the generation and evolution of nonlinear internal waves in the South China Sea. *J. Geophys. Res.* **115**, C02012.

CAI, S., LONG, X. & GAN, Z. 2002 A numerical study of the generation and propagation of internal solitary waves in the Luzon Strait. *Oceanol. Acta* **25**, 51–60.

CHEN, G.-Y., LIU, C.-T., WANG, Y.-H. & HSU, M. K. 2011 Interaction and generation of long-crested internal solitary waves in the South China Sea. *J. Geophys. Res.* **116**, C06013.

CUMMINS, P. F. & ARMI, L. 2010 Upstream internal jumps in stratified sill flow: observations of formation. *J. Phys. Oceanogr.* **40**, 1419–1426.

CUMMINS, P. F., ARMI, L. & VAGLE, S. 2006 Upstream internal hydraulic jumps. *J. Phys. Oceanogr.* **36**, 753–769.

CUMMINS, P., VAGLE, S., ARMI, L. & FARMER, D. 2003 Stratified flow over topography: upstream influence and generation of nonlinear internal waves. *Proc. R. Soc. Lond.* A **459**, 1467–1487.

DUDA, T. F., LYNCH, J. F., IRISH, J. D., BEARDSLEY, R. C., RAMP, S. R., CHIU, C. S., TANG, T. Y. & YANG, Y. J. 2004 Internal tide and nonlinear internal wave behavior at the continental slope in the northern South China Sea. *IEEE J. Ocean. Engng* **29**, 1105–1130.

FARMER, D. M. & ARMI, L. 1999*a* The generation and trapping of solitary waves over topography. *Science* **283**, 188–190.

FARMER, D. M. & ARMI, L. 1999*b* Stratified flow over topography: the role of small scale entrainment and mixing in flow establishment. *Proc. R. Soc. Lond.* A **455**, 3221–3258.

FARMER, D. M. & ARMI, L. 2001 Stratified flow over topography: models versus observations. *Proc. R. Soc. Lond.* A **457**, 267–280.

https://doi.org/10.1017/jfm.2018.21 Published online by Cambridge University Press

FARMER, D. M. & SMITH, J. D 1980 Tidal interaction of stratified flow with a sill in Knight Inlet. *Deep-Sea Res.* A **27**, 239–254.

GERKEMA, T. 2001 Internal and interfacial tides: beam scattering and local generation of solitary waves. *J. Mar. Res.* **59**, 227–255.

GRIMSHAW, R. 2010 Transcritical flow past an obstacle. *ANZIAM J.* **52**, 1–25.

GRIMSHAW, R., PELINOVSKY, E. & TALIPOVA, T. 2007 Modeling internal solitary waves in the coastal ocean. *Surv. Geophys.* **28**, 273–298.

GRIMSHAW, R., PELINOVSKY, E., TALIPOVA, T. & KURKINA, A. 2010 Internal solitary waves: propagation, deformation and disintegration. *Nonlinear Process. Geophys.* **17**, 633–649.

GRIMSHAW, R. H. J. & SMYTH, N. F 1986 Resonant flow of a stratified fluid over topography. *J. Fluid Mech.* **169**, 429–464.

GUO, C., CHEN, C., VLASENKO, V. I. & STASHCHUK, N. 2011 Numerical investigation of internal solitary waves from the Luzon Strait: generation process, mechanism and three-dimensional effects. *Ocean Model.* **38**, 203–216.

HELFRICH, K. R. & MELVILLE, W. K. 2006 Long nonlinear internal waves. *Annu. Rev. Fluid Mech.* **38**, 395–425.

HIBIYA, T. 1988 The generation of internal waves by tidal flow over Stellwagen Bank. *J. Geophys. Res.* **93**, 533–542.

HOLLOWAY, P., PELINOVSKY, E. & TALIPOVA, T. 2001 Internal tide transformation and oceanic internal solitary waves. In *Environmental Stratified Flows* (ed. R. Grimshaw), pp. 31–60. Kluwer.

LAI, Z., CHEN, C., COWLES, G. W. & BEARDSLEY, R. C. 2010 A nonhydrostatic version of FVCOM. Part 2. Mechanistic study of tidally generated nonlinear internal waves in Massachusetts Bay. *J. Geophys. Res.* **115**, C12049.

LEE, C.-Y. & BEARDSLEY, R. C. 1974 The generation of long nonlinear internal waves in weakly stratified shear flows. *J. Geophys. Res.* **79**, 453–462.

LI, Q. & FARMER, D. M. 2011 The generation and evolution of nonlinear internal waves in the deep basin of the South China Sea. *J. Phys. Oceanogr.* **41**, 1345–1363.

LIU, A. K., CHANG, Y. S., HSU, M. K. & LIANG, N. K. 1998 Evolution of nonlinear internal waves in the East and South China Seas. *J. Geophys. Res.* **103**, 7995–8008.

LIU, A. K., RAMP, S. R., ZHAO, Y. & TSWEN YUNG TANG, T. Y. 2004 A case study of internal solitary wave propagation during ASIAEX 2001. *IEEE J. Ocean. Engng* **29**, 1144–1156.

LIU, CH-T, PINKEL, R., KLYMAK, J., HSU, M. K., CHEN, H. W. & VILLANOY, C. 2006 Nonlinear internal waves from the Luzon Strait. *EOS* **87**, 449–451.

MAXWORTHY, T. 1979 A note on the internal solitary waves produced by tidal flow over a three-dimensional ridge. *J. Geophys. Res.* **84**, 338–346.

MELVILLE, W. K. & HELFRICH, K. R. 1987 Transcritical two-layer flow over topography. *J. Fluid Mech.* **178**, 31–52.

ORR, M. H. & MIGNEREY, P. C. 2003 Nonlinear internal waves in the South China Sea: observation of the conversion of depression internal waves to elevation internal waves. *J. Geophys. Res.* **108(C3)**, 3064.

RAMP, S. R., TANG, T. Y., DUDA, T. F., LYNCH, J. F., LIU, A. K., CHIU, C. S., BAHR, F. L., KIM, H. R. & YANG, Y. J. 2004 Internal solitons in the northeastern South China Sea. Part I. Sources and deep water propagation. *IEEE J. Ocean. Engng* **29**, 1157–1181.

REDEKOPP, L. G. & YOU, Z. 1995 Passage through resonance for the forced Korteweg–de Vries equation. *Phys. Rev. Lett.* **74**, 5158–6161.

SCOTTI, A., BEARDSLEY, R. C. & BUTMAN, B. 2007 Generation and propagation of nonlinear internal waves in Massachusetts Bay. *J. Geophys. Res.* **112**, C10001.

SCOTTI, A., BEARDSLEY, R. C., BUTMAN, B. & PINEDA, J. 2008 Shoaling of nonlinear internal waves in Massachusetts Bay. *J. Geophys. Res.* **113**, C08031.

STASHCHUK, N. & VLASENKO, V. I. 2007 Numerical modelling of stratified tidal flow over a fjord sill. *Ocean Dyn.* **57**, 325–338.

STASTNA, M. & PELTIER, W. R. 2004 Upstream-propagating solitary waves and forced internal-wave breaking in stratified flow over a sill. *Proc. R. Soc. Lond.* A **460**, 3159–3190.

https://doi.org/10.1017/jfm.2018.21 Published online by Cambridge University Press

STASTNA, M. & PELTIER, W. R. 2005 On the resonant generation of large-amplitude internal solitary and solitary-like waves. *J. Fluid Mech.* **543**, 267–292.

VLASENKO, V. I., GUO, C. & STASHCHUK, N. 2012 On the mechanism of A-type and B-type internal solitary wave generation in the northern South China Sea. *Deep-Sea Res.* I **69**, 100–112.

VLASENKO, V. I., STASHCHUK, N., GUO, C. & CHEN, X. 2010 Multimodal structure of baroclinic tides in the South China Sea. *Nonlinear Process. Geophys.* **17**, 529–543.

WARN-VARNAS, A., HAWKINS, J., LAMB, K. G., PIACSEK, S., CHIN-BING, S., KING, D. & BURGOS, G 2010 Solitary wave generation dynamics at Luzon Strait. *Ocean Model.* **31**, 9–27.

WILLIAMSON, J. H. 1980 Low-storage Runge–Kutta schemes. *J. Comput. Phys.* **35**, 48–56.

ZHAO, Z. & ALFORD, M. H. 2006 Source and propagation of internal solitary waves in the northeastern South China Sea. *J. Geophys. Res.* **111**, C11012.

https://doi.org/10.1017/jfm.2018.21 Published online by Cambridge University Press